

# Cosmological N-Body Simulations

J.S.Bagla and T.Padmanabhan  
Inter-University Centre for Astronomy and Astrophysics,  
Post Bag 4, Ganeshkhind, Pune 411 007, INDIA

## Abstract

In this review we discuss Cosmological N-Body codes with a special emphasis on Particle Mesh codes. We present the mathematical model for each component of N-Body codes. We compare alternative methods for computing each quantity by calculating errors for each of the components. We suggest an optimum set of components that can be combined reduce overall errors in N-Body codes.

## 1 Introduction

Observations suggest that the present universe is populated by very large structures like galaxies, clusters of galaxies etc. Current models for formation of these structures are based on the assumption that gravitational amplification of small perturbations leads to the formation of large scale structures. In absence of analytical methods for computing quantities of interest, numerical simulations are the only tool available for study of clustering in the non-linear regime. The last two decades have seen a rapid development of techniques and computing power for cosmological simulations and the results of these simulations have provided valuable insight into the study of structure formation. In this paper we will describe some aspects of the cosmological N-body simulation, based on the code developed and used by the authors. We will stress the key physical and numerical ideas and detail some useful tests of the N-Body code. After an initial introduction to cosmological N-Body codes the discussion of N-Body codes will focus on Particle Mesh [PM] codes. [For a comprehensive discussion of numerical simulations using particles, see Hockney and Eastwood (1988).]

An N-body code consists of two basic modules: one part computes the force field for a given configuration of particles and the other moves the particles in this force field. These two are called at each step to ensure that the force field and the particle trajectories evolve in a self consistent manner. Apart from these we also need to setup the initial conditions and write the output. Thus the basic plan of an N-Body code follows the flow chart shown in figure 1.

Structure of these modules depends on the specific application at hand. Here we outline some features that are particular to cosmological N-Body codes. To make quantitative statements about the required parameters of an N-Body simulation we shall assume that the particles populate a region of volume  $V$ . We shall also assume that we are using  $N_p$  particles to describe the density field. The following physical requirements have to be taken into account while writing cosmological N-Body codes.

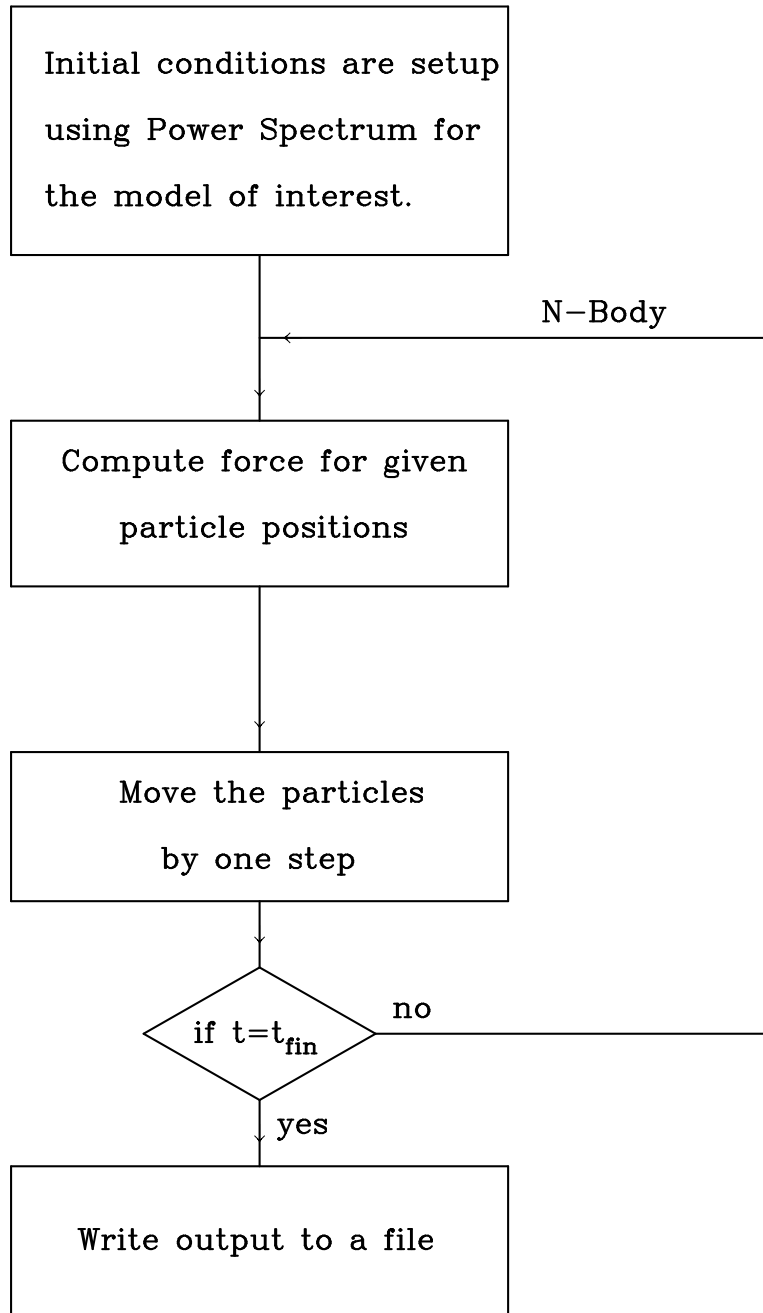


Figure 1: Flow chart for an N-Body Code.

The universe is filled with matter over scales that are much larger than the scales of interest in an N-Body simulation. Density averaged over larger and larger scales in the universe approaches a constant value. Thus the simulation volume  $V$  can not be assumed to exist in isolation and we must fill the region outside this volume by some method. Periodic boundary conditions are the only viable solution to this problem. In absence of periodic boundary conditions most of the matter in the simulation volume has a tendency to collapse towards the centre of the box, giving rise to a spurious, large rate of growth for perturbations. [A compromise solution, called quasiperiodic boundary conditions, has been tried to solve this problem for tree codes. In this scheme periodic boundary conditions are used to restructure the simulation volume to bring a particle at the centre of the box while computing force at its position. This is done for each particle so that there is no strong tendency to collapse towards the centre of the box. (Bouchet and Hernquist (1988))] The most natural geometry for a volume with periodic boundary conditions is a cube.

We would like the evolution of perturbations to be independent of the specific boundary conditions. Thus the simulation volume should not be dominated by any one object. [If the simulation volume is dominated by one object then the tidal force due to its own periodic copies will influence its later evolution.]

We require the average density in the box to equal the average density of the universe. Thus perturbations averaged at the scale of the box must be ignorable at all times for the model of interest, i.e.,  $(\delta = V^{-1/3}) \ll 1$ . [Here  $(\delta)$  is the rms dispersion in the mass averaged at scale  $R$ .] For example, in case of the standard CDM model this would require the box to be at least  $100h^{-1}\text{Mpc}$  [at  $z = 0$ ] in extent.

We would like to probe scales that are sufficiently non-linear in order to justify the use of N-Body simulations. If we wish to compare the results with the real universe then we should be able to study the formation of structures with a large range in scales. In other words, the mass of individual particles in an ideal simulation must be less than the mass of the smallest structure of interest. Therefore the smallest number of particles required to cover the relevant range of scales to study galaxy clustering, say, is

$$N = \frac{M(100h^{-1}\text{Mpc})}{M_{\text{galaxy}}} \approx \frac{5 \cdot 10^8 M_{\odot}}{10^{11} M_{\odot}} \approx 5 \cdot 10^7 \quad (1)$$

We need a very large number of particles to represent the density field over this range of scales. Therefore most numerical techniques used in cosmological N-Body codes are oriented towards reducing the number of operations and stored quantities per particle.

We approximate collection of a very large number of particles in the universe by one particle in an N-Body simulation. Therefore the particles in an N-Body simulation must interact in a purely collisionless manner.

The periodic boundary conditions and a very large number of particles are the key considerations in developing the detailed algorithm for an N-Body code. Of the two main components in an N-Body

code, integration of the equation of motion is a process of order  $O(N_p)$ . The calculation of force, if done by summing the force over all pairs, is a process of order  $O(N_p^2)$ . Therefore the calculation of force is likely to be more time consuming than evolving the trajectories in N-Body codes with a large number of particles. It can be shown that, for particle numbers greater than a few hundred, direct computation of force takes an excessively long time even on the fastest computers. [The very high speed special purpose computers are an exception to this. (Brieu (Summers and Ostriker))] Three schemes have been evolved to address this problem and replace direct summation over pairs by methods that are less time consuming. These are

*Particle Mesh (PM)* : Poisson equation is solved in the Fourier domain and the potential/force is computed on a fixed grid. The force is then interpolated to particle positions for moving the particles. Density field, the source for gravitational potential, is also computed on the same mesh/grid from particle positions by using a suitable interpolating function. The “smoothing” of particles limits the resolution of such simulations but ensures collisionless evolution. [See Bouchet, Adam and Pellat (1984) and Bouchet and Kandrup, (1985) for an excellent discussion of PM codes.]

*Particle-Particle Particle Mesh (P<sup>3</sup>M)* : This scheme (Efstathiou et al, 1985) improves the resolution of PM method by adding a correction to the mesh force for pairs of particles with separation of the order of, and smaller than, the grid length. The number of operations required for this correction is proportional to  $N_p n(R)$  where  $n(R)$  is the average number of neighbouring particles within a distance  $R$ . This can be written as  $N_p n(1 + \xi(R))$ , where  $n$  is the average number density and  $\xi$  is the averaged correlation function. It is obvious that such corrections can become time consuming in highly clustered situations [when  $\xi(R) \gg 1$ ].

*Tree* : In this scheme, information about the density field is set up in form of a hierarchical tree. Each level of the tree specifies position of the centre of mass and the total mass for a region in the simulation volume. Force from particles in distant regions in the simulation box is approximated by the force from the centre of mass for particles in that region. This leads to a reduction in the number of operations required for calculating force. [Barnes and Hut (1986); Bouchet and Hernquist (1988)] To estimate the number of operations required for setting up the tree structure and evaluate the force, let us assume that the simulation volume is a cube and is subdivided into eight equal parts at each level. This subdivision of cells is continued till we have at most one particle per cell at the smallest level. Each particle is parsed at most once at each level, therefore the upper bound on the total number of operations is proportional to  $N_p \ln(L_{\text{box}}/l_{\text{min}})$  where  $l_{\text{min}}$  is the smallest inter-particle separation for the given distribution of particles. We have,

$$l_{\text{min}} \sim n_{\text{max}}^{-1/3} = n_{\text{max}}^{-1/3} n^{1/3} = N_p^{-1/3} L_{\text{box}} n_{\text{max}}^{-1/3} \quad (2)$$

where  $n$  is the average number density,  $n_{\text{max}}$  is the maximum density contrast and  $n_{\text{max}}$  is the highest number density in the given distribution of particles. This implies that the upper bound on number of operations is proportional to  $O(N_p \ln N_p n_{\text{max}})$ . Incorporating periodic boundary conditions is a very nontrivial problem in the context of tree codes. [See Hernquist, Bouchet and Suto (1991) for a discussion of periodic boundary conditions for tree codes.]

Amongst these methods the PM scheme has two advantages over the other methods. Firstly it is the only one of the three methods outlined above that ensures a collisionless evolution. [See Melott et al. (1997); Suisalu and Saar (1996).] Secondly it has the simplest algorithm and it is also the fastest of the three methods discussed above. In the remaining discussion we shall focus only on PM codes. However, apart from computation of force, all other components are the same in all these codes [with some minor variations] and most of the conclusions about relative merits of the available alternatives are applicable for all three types of codes.

## 2 Moving the Particles

In this section we will first present the system of equations that describe the evolution of trajectories of particles. This will be followed by a description of the methods used for numerical integration of equation of motion.

### 2.1 Equation of Motion

It can be shown that the evolution of perturbations in a non-relativistic medium in an expanding background can be studied in the Newtonian limit at scales that are much smaller than the Hubble radius  $d_H = c/H_0$ . The equations for a set of particles interacting only through the gravitational force can be written as

$$\begin{aligned} \ddot{x} + 2\frac{\dot{a}}{a}\dot{x} &= -\frac{1}{a^2}r_x' \\ r_x'^2 &= 4G a^2 \rho = \frac{3}{2}H_0^2 \Omega_0 \frac{1}{a} \end{aligned} \quad (3)$$

Here the last equality follows from the Friedmann equations that describe evolution of the scale factor for the universe. The variables used here are : comoving co-ordinates  $x$ , time  $t$ , scale factor  $a$ , gravitational potential due to perturbations  $\phi$ , density  $\rho$  and density contrast  $\delta$ . Cosmological parameters used in this equation are : the Hubble's constant  $H_0$  and the density parameter contributed by non-relativistic matter  $\Omega_0$ .

N-Body simulations integrate this equation numerically for each particle. Numerical integration can be simplified by modifying the equation of motion so that the velocity dependent term is removed from the equation of motion. This can be achieved by using a different time parameter (Klypin and Shandarin (1983)). This is defined as

$$d = H_0 \frac{dt}{a^2} \quad (4)$$

In terms of which we have

$$\begin{aligned} \frac{d^2 x}{d^2} &= -\frac{3}{2} \Omega_0 a^2 r \\ r^2 &= - \end{aligned} \quad (5)$$

In this form, all the cosmological factors can be clubbed in the source term in the equation of motion, making numerical implementation much simpler.

## 2.2 Numerical Integration

In any N-Body code, a great deal of computer time is devoted to integration of the equation of motion. The basic idea of time integration is simple : the equation of motion expresses the second derivative of position in terms of position, velocity and time. Time integration translates this into the subsequent changes in position and velocity. In the following discussion we will develop the idea of numerical integration of trajectories.

Writing the position and velocity at time  $t + \Delta t$  in a Taylor series about the position and velocity at time  $t$ , we have

$$\begin{aligned}x_i(t + \Delta t) &= x_i(t) + v_i(t) \Delta t + \frac{1}{2} a_i(t) \Delta t^2 + \dots \\v_i(t + \Delta t) &= v_i(t) + a_i(t) \Delta t + \frac{1}{2} j_i(t) \Delta t^2 + \dots\end{aligned}\quad (6)$$

Here  $x$  is the position,  $v$  is the velocity,  $a$  is the acceleration and  $j$  is the rate of change of acceleration, and the subscript is used to identify the particle. We can use the equation of motion to express acceleration and the higher derivatives of position in terms of positions and velocities. Therefore, in principle, we can find the new position and velocity with arbitrary accuracy. However, such a scheme is not very practical from the computational point of view as it requires an infinite series to be summed. A more practical method consists of truncating the series at some point and using sufficiently small time steps to ensure the required level of accuracy. To illustrate this point, let us consider terms up to first order in the above series, we get

$$\begin{aligned}v_i(t + \Delta t) &= v_i(t) + a_i(t) \Delta t + O(\Delta t^2) \\x_i(t + \Delta t) &= x_i(t) + v_i(t) \Delta t + O(\Delta t^2)\end{aligned}\quad (7)$$

This is the Euler's method of solving differential equations and the error in the solution is of order  $\Delta t^2$ . Thus choosing a smaller time step leads to smaller error in each step. However, the number of steps required to integrate over a given interval in time is inversely proportional to the time step so that the overall error changes only linearly with step size.

Let us consider terms up to  $\Delta t^2$  in order to devise a more accurate integrator.

$$\begin{aligned}x_i(t + \Delta t) &= x_i(t) + v_i(t) \Delta t + \frac{1}{2} a_i(t) \Delta t^2 + O(\Delta t^3) \\v_i(t + \Delta t) &= v_i(t) + a_i(t) \Delta t + \frac{1}{2} j_i(t) \Delta t^2 + O(\Delta t^3)\end{aligned}\quad (8)$$

This equation contains the rate of change of acceleration and therefore is not very useful in this form. To simplify these equations without losing accuracy, let us specify  $j$  as

$$j(t) = \frac{a(t + \Delta t) - a(t)}{\Delta t} + O(\Delta t)\quad (9)$$

This reduces the above equations to the following form

$$\begin{aligned}x_i(t + \Delta t) &= x_i(t) + v_i(t) \Delta t + \frac{1}{2} a_i(t) \Delta t^2 + O(\Delta t^3) \\v_i(t + \Delta t) &= v_i(t) + \frac{\Delta t}{2} (a_i(t) + a_i(t + \Delta t)) + O(\Delta t^3)\end{aligned}\quad (10)$$

|       | $(x)_{\text{rms}}$  |
|-------|---------------------|
| 0.1   | $5.4 \cdot 10^{-4}$ |
| 0.05  | $7.3 \cdot 10^{-5}$ |
| 0.02  | $3.5 \cdot 10^{-5}$ |
| 0.01  | $1.2 \cdot 10^{-5}$ |
| 0.005 | $5.3 \cdot 10^{-6}$ |

Table 1: This table lists the values of  $\Delta t$  used in forward and backward integration of trajectories of a set of particles in an external potential and the corresponding error in recovering the initial conditions. Here we have used one grid length as the unit of length.

This method can be used for velocity independent forces and is identical to the Leap-Frog method. The standard Leap-Frog method involves updating the velocity and position at an offset of half a step. To see the equivalence of the above equations and the Leap-Frog method let us consider the expressions for velocity at  $t + \Delta t = 2$  and  $t - \Delta t = 2$ .

$$\begin{aligned} v_i(t + \Delta t = 2) &= v_i(t) + \frac{\Delta t}{2} a_i(t) + \frac{1}{8} \Delta t^2 j_i(t) + O(\Delta t^3) \\ v_i(t - \Delta t = 2) &= v_i(t) - \frac{\Delta t}{2} a_i(t) + \frac{1}{8} \Delta t^2 j_i(t) + O(\Delta t^3) \end{aligned} \quad (11)$$

These two equations can be combined to give

$$v_i(t + \Delta t = 2) = v_i(t - \Delta t = 2) + \Delta t a_i(t) + O(\Delta t^3) \quad (12)$$

We can also use the expression for velocity at  $(t + \Delta t)$  to write

$$x_i(t + \Delta t) = x_i(t) + v_i(t + \Delta t = 2) + O(\Delta t^3) \quad (13)$$

These two equations can now be combined to give the Leap-Frog method.

$$\begin{aligned} x_i(t + \Delta t) &= x_i(t) + v_i(t + \Delta t = 2) + O(\Delta t^3) \\ v_i(t + 3 \Delta t = 2) &= v_i(t + \Delta t = 2) + \Delta t a_i(t) + O(\Delta t^3) \end{aligned} \quad (14)$$

This is called the Leap-Frog method as it updates velocities halfway between the step that is used to update the position. For velocity dependent forces these methods have to be modified into a predictor-corrector form.

It is possible to improve the accuracy by using integrators that retain more terms in the Taylor series expansion. However most of these schemes require many evaluations of force for each step making them computationally uneconomical.

### 2.3 Choosing the Time Step

The time step for integrating the equation of motion can be chosen in many ways. In all of these methods one defines a suitable criterion [like energy conservation] and then obtains the largest time step that will satisfy the requirement. Following is a list of possible criteria :

Monitoring validity of Irvine-Layzer equation. This is done by integrating the Irvine-Layzer equation [Irvine (1961); Layzer (1963); Dmitriev and Zel'dovich (1964)]

$$T + U + \int^z \frac{da}{a} (2T + U) = C \quad (15)$$

and monitoring the constant  $C$ . Variation in  $C$  with respect to total energy  $T + U$  can be used as an indicator of non conservation. [This is normally done with different forms of this equation so that only the kinetic or the potential energy term contributes to the integral. (Efstathiou et al. (1985))] In schemes where the force is computed at mesh points and then interpolated to particle positions the force at the particle position,  $f(\mathbf{x}) \neq -\nabla\phi(\mathbf{x})$ , i.e., the force does not equal the gradient of potential at a point. This leads to an apparent non conservation of energy. If we include a correction term in the energy equation to account for this fact (Efstathiou et al. (1985)) then it can be shown that it is possible to improve conservation of energy. This correction involves a direct sum over all pairs of particles and is therefore an almost impossible task to implement for a simulation with a large number of particles. Thus this is not a practical method of deciding the time step.

Convergence of final positions and velocities. If we evolve the trajectories of a set of particles with different time steps, then we expect the final positions and velocities to converge towards the correct value as we reduce the time step. This can be used to decide the time step.

Reproducibility of initial conditions. This is a more stringent version of the test outlined above. This method ensures that the solution we get is correct and errors are not building up systematically. If we run the particles forward and then back again we should in principle get back the initial positions. Although we ignore the decaying mode while integrating trajectories forward in time, it tends to dominate if we evolve the system in the opposite direction. We can overcome this difficulty by not evolving the potential during this test.

We find the last test to be the most stringent one and we use it to fix the time step for an arbitrary potential by the following construct. Consider an arbitrary potential which has the maximum value of the magnitude of its gradient as  $g_{max} = |\nabla\phi|_{max}$ . We can write the equation of motion eqn.(5) for a small interval as

$$\frac{1}{2} \dot{x}^2 = \frac{24}{4} g_{max} \Delta x \quad (16)$$

Here we have used  $\Delta x$  to represent the largest displacement in time  $\Delta t$ . We have specialised to  $\dot{x}_0 = 1$  in writing the above equation. In which case,  $\Delta t = \sqrt{\frac{24}{4} \frac{\Delta x}{g_{max}}}$ . For a given value of  $\Delta x$  we can fix the time step as

$$\Delta t = \sqrt{\frac{24}{4} \frac{\Delta x}{g_{max}}} \quad (17)$$

We can use the test mentioned above to fix the value of  $\Delta t$ . Table 1 lists a few values of  $\Delta t$  and  $(\Delta x)_{rms}$  for a CDM simulation [boxsize=64h<sup>-1</sup>Mpc] with 64<sup>3</sup> particles in a 64<sup>3</sup> box. The system was evolved from  $a = 0.02$  to 0.25 and then back to  $a = 0.02$ . We use  $\Delta t = 0.005$  for our simulations as we find the error in this case to be acceptable.

### 3 Calculating the Force

An N-Body code solves the equation of motion and the Poisson equation in a self consistent manner. Therefore, moving the particles and computing the force for a given distribution of particles are the two most important components of an N-Body code. In this section we will discuss computation of force at mesh points for a given distribution of particles. For simplicity we shall assume that all the particles have the same mass. Generalisation to particles with different masses is not difficult but can strain the resources like RAM. [Setting up initial conditions for simulations that have particles with different masses is much simpler than setting up initial conditions for simulations that use particles with equal mass. See x4 for details.]

In particle mesh codes the force at the particle position can be computed from the potential defined at mesh points in two ways. These are :

*Energy Conserving Schemes* : The force is computed at particle positions by using the gradient of the interpolating function.

$$f(\mathbf{x}) = -\sum_{\mathbf{x}_i} \nabla_{\mathbf{x}} W(\mathbf{x}; \mathbf{x}_i) \rho(\mathbf{x}_i) \quad (18)$$

The sum is over all the mesh points. An additional requirement is that the same interpolating function  $W$  should be used to compute the density field on the mesh from the distribution of particles. These are called energy conserving schemes as the force and gravitational potential are related to each other as  $f(\mathbf{x}) = -\nabla_{\mathbf{x}} \phi(\mathbf{x})$ .

*Momentum Conserving Schemes* : The force is computed on the mesh and then interpolated to the particle position.

$$f(\mathbf{x}) = \sum_{\mathbf{x}_i} \nabla_{\mathbf{x}} W(\mathbf{x}; \mathbf{x}_i) \rho(\mathbf{x}_i) \quad (19)$$

Momentum conserving schemes also require the same interpolating function to be used for computing density field on the mesh. It can be shown that in these schemes the force due to the  $i$ th particle on the  $j$ th particle is same as the force due to  $j$ th particle on the  $i$ th particle. [ $f_{ij} = -f_{ji}$ .] This clearly is a necessary condition for momentum conservation.

Use of mesh leads to anisotropy in force at scales comparable to the mesh size. A simple method for limiting these anisotropies is to choose a configuration that leads to a softer force at the mesh scale. Collisionless evolution also requires the force to drop rapidly below the average inter-particle separation (Melott et al. (1997)). We choose to work with the momentum conserving schemes as these lead to a softer force at small scales in comparison with the energy conserving schemes.

The algorithm for computing force at particle positions involves the following major steps.

*Computing the Density Field* : Mass of particles is assigned to mesh points by using an interpolating function. Density contrast is calculated from this “mass field” by using the definition

$$\delta = \frac{\rho - \bar{\rho}}{\bar{\rho}} \quad (20)$$

Here  $M$  is the average mass per mesh point. Then fast Fourier transform technique is used to compute the Fourier components of density contrast.

*Solving the Poisson Equation* : The Poisson equation is solved in Fourier space. The FFT can be used to compute the gravitational potential on the mesh.

*Computing the Force* : The gravitational force equals the negative gradient of the gravitational potential, therefore the next step in algorithm is computing the gradient of potential. This can be done either in Fourier space or in real space by using some scheme for numerical differentiation. Force at the particle positions is computed by interpolation from the mesh points.

In the following subsections we will discuss each of these steps in greater detail.

### 3.1 Computing the Density Contrast

Smoothing [interpolating] functions are used to assign mass to the lattice points for a given configuration of particles. This is done by computing the following sum for every mesh point.

$$M(\mathbf{x}_i) = \sum_{\text{all particles}} M_{\text{particle}} W(\mathbf{x}; \mathbf{x}_i) \quad (21)$$

Here  $\mathbf{x}_i$  are the co-ordinates of mesh points,  $\mathbf{x}$  are the coordinates of particles and  $W$  is the interpolating function. As we have assigned same mass to all the particles we can scale the mass at mesh sites with the particle mass.

Density contrast is computed from the mass defined at mesh points by using eqn.(20). FFT is then used to compute its Fourier transform.

The smoothing function  $W$  should satisfy certain algebraic, computational and physical requirements.

The sum of weights given to lattice points should equal unity. The interpolating function should be continuous and preferably differentiable as well.

The smoothing function should be peaked at small separations and should decay rapidly at large separations. The smoothing function should have the smallest possible base, i.e., the number of lattice separations over which it is non-zero should be small. The number of arithmetic operations required for interpolation is proportional to the cube of the number of lattice cells over which the interpolating function is non-zero.

The interpolating function should be isotropic.

It is clear that we can not satisfy all these criteria fully and at the same time and therefore we have to consider a compromise solution. The first simplification that is made is to break up the three dimensional interpolating function into a product of three one dimensional interpolating functions. This reduces the complexity of the problem but also implies that the interpolating function cannot be manifestly isotropic.

These considerations, and the above mentioned simplifying assumption then leads to the following set of interpolating functions.

*Nearest Grid Point* [NGP] : This is the simplest interpolating function. In this assignment scheme all the mass is assigned to the nearest grid point.

$$W(x; x_i) = \begin{cases} 1 & (\text{for } |x - x_i| \leq L/2) \\ 0 & (\text{for } |x - x_i| > L/2) \end{cases} \quad (22)$$

where  $L$  is the grid spacing. This clearly satisfies the algebraic condition that the sum of weights should equal unity. However, this function is neither continuous nor differentiable. The leading term in the error in force of a point mass computed using this mass assignment scheme has a dipole like behaviour.

*Cloud In Cell* [CIC] : This the most commonly used interpolating function. Linear weights are used and mass is assigned to the two nearest grid points. The function is continuous but not differentiable.

$$W(x; x_i) = \begin{cases} \frac{x - x_{i-L}}{L} & (\text{for } |x - x_i| \leq L) \\ \frac{x_i - x}{L} & (\text{for } |x - x_i| > L) \\ 0 & (\text{elsewhere}) \end{cases} \quad (23)$$

*Triangular Shaped Cloud* [TSC] : The third function we wish to discuss is a quadratic spline that is continuous and also has a continuous first derivative. In this case the mass is distributed over three lattice points in each direction.

$$W(x; x_i) = \begin{cases} \frac{3}{4} \left( \frac{x - x_i}{L} \right)^2 & (\text{for } |x - x_i| \leq L/2) \\ \frac{3}{8} \left( 1 - \frac{2|x - x_i|}{3L} \right)^2 & (\text{for } L/2 < |x - x_i| \leq 3L/2) \\ 0 & (\text{for } |x - x_i| > 3L/2) \end{cases} \quad (24)$$

Here  $|x - x_i|$  is the magnitude of separation between the particle and the mesh point. This function satisfies the requirements from the physical point of view but it is generally considered expensive from the computational point of view.

It is obvious that these smoothing functions become more and more computationally intensive as we go for a larger base. All of the functions described above satisfy the essential algebraic requirements, so that the final choice is a compromise between the accuracy of the force field obtained using these and the computational requirements. However, we do not go beyond TSC as the base becomes very large and the transverse error in force becomes unacceptably large.

Figure 2 compares these smoothing functions in a realistic situation. We have plotted the average weight assigned to a point that is at a distance  $r$  from the mesh point of interest. The curve in each of the panels shows the average weight where the average is computed over all directions  $[\theta; \phi]$  while keeping  $r$  fixed. The vertical bars show the *rms* dispersion about this average to depict the level of anisotropies in each of these functions. It is clear that TSC is the most isotropic of these functions and CIC is a “reasonable” compromise between isotropy and computational requirements. We will use the TSC smoothing function in the N-Body code for all applications.

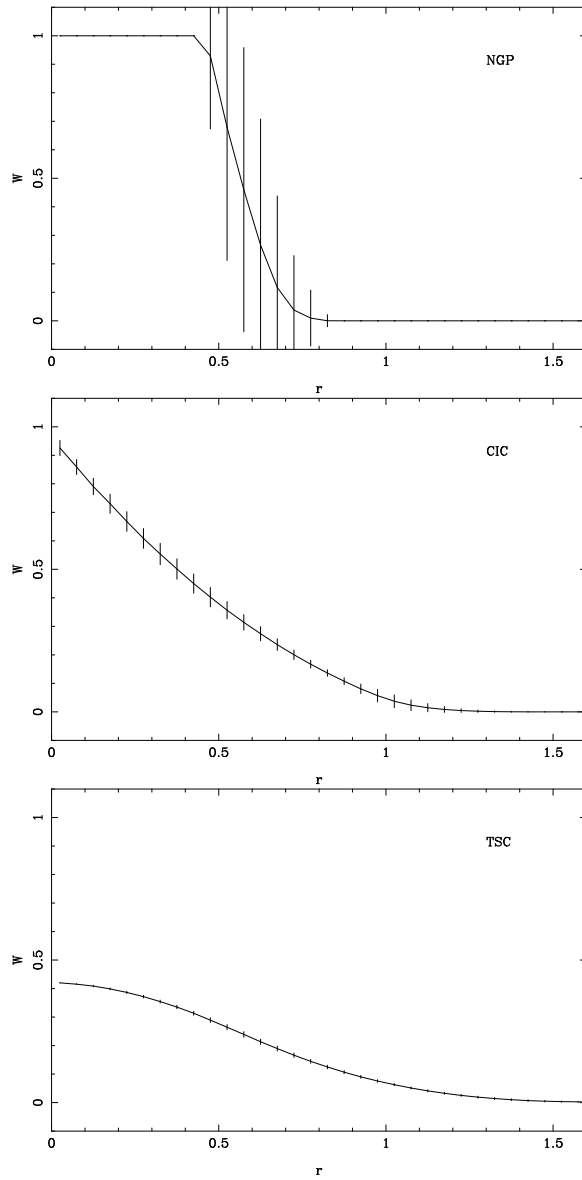


Figure 2: This figure shows the weight assigned to a point that is at a distance  $r$  from the mesh point of interest. The curve in each of the panels shows the average weight where the average is computed over all directions  $[\theta; \phi]$ , keeping  $r$  fixed. The vertical bars show the *rms* dispersion about this average to depict the level of anisotropies in these functions.

### 3.2 Solving the Poisson Equation

The equation we wish to solve is

$$\nabla^2 \phi = -\frac{\rho}{\epsilon_0} \quad (25)$$

This equation is to be solved with periodic boundary conditions. In particle mesh codes the equation is solved in the Fourier space. To solve this equation with periodic boundary conditions we must ensure that only the harmonics of the fundamental wave number  $k_F = 2\pi/L$  contribute to the function. [ $L$  is the size of the simulation box.] This type of sampling of  $k$  space is also required by the fast Fourier transforms. Therefore as long as we use FFT for computing Fourier transforms the correct boundary conditions are automatically incorporated.

Two types of Green's functions are commonly used for solving the Poisson equation in Fourier space. These are

*Poor Man's Poisson Solver* : This method uses the continuum Green's function.

$$\begin{aligned} \phi(\mathbf{k}) &= \frac{\rho(\mathbf{k})}{\epsilon_0 k^2} \\ G(\mathbf{k}) &= \frac{1}{k^2} \end{aligned} \quad (26)$$

The main advantage of this is that it is the true Green's function. Also, it is isotropic by construction.

*Periodic Green's Function* : An alternative is to substitute Fourier transform of a discrete realisation of the Laplacian. A Green's function derived in this manner tends to increase power at small scales and leads to larger anisotropies in the force field. A commonly used Green's function of this class is

$$G(\mathbf{k}) = \frac{L^2}{4 \sin^2 k_x L + 4 \sin^2 k_y L + 4 \sin^2 k_z L} \quad (27)$$

Here  $L$  is the grid spacing and equals unity in the units that we are using here. This Green's function is invariant under the transformation  $k_x \rightarrow k_x + 2\pi/L$ . All FFT routines use such a transformation to rearrange wave modes for ease of manipulation [See §3]. Therefore this Green's function is easier to implement as compared to the continuum version as one does not have to worry about the rearrangement of wave modes. The main disadvantage of this Green's function is that it is anisotropic at small scales.

We have plotted the two Green's functions in figure 3. Like figure 2 the curve here shows the average over angular coordinates for any value of  $k = |\mathbf{k}|$ . The vertical bars show the *rms* dispersion about this average and are an indicator of anisotropy. It is clear from this figure that the periodic Green's function enhances power at small scales, beyond the true value, and also introduces some anisotropy in the potential.

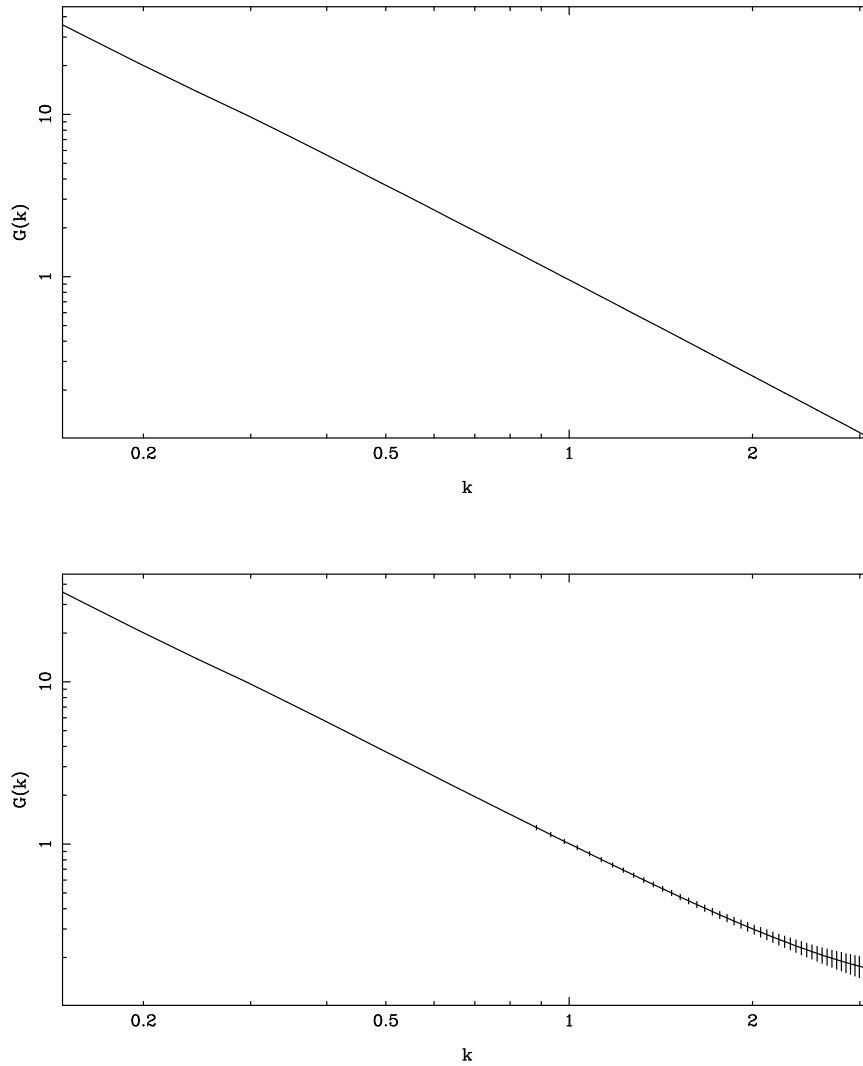


Figure 3: This figure shows the two Green's functions described in the text. Upper panel shows the continuum Green's function and the lower panel shows the Green's function derived from discrete representation of the Laplacian. Curves in each panel show the average of  $G(k)$  over angular coordinates for any value of  $k = |k|$ . The vertical bars show the  $rms$  dispersion about this average and are an indicator of anisotropy.

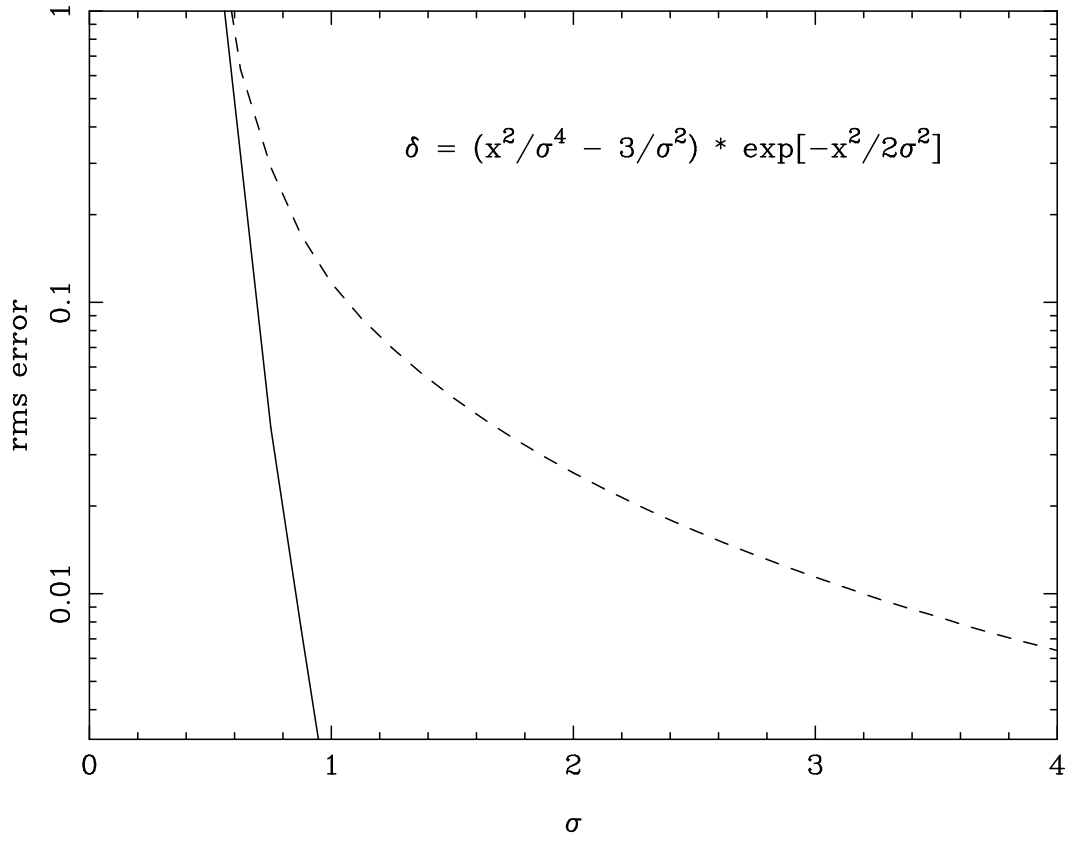


Figure 4: This figure shows the *rms* error in solving Poisson equation as a function of the parameter defined in the text. The dashed line shows the error for the periodic kernel whereas the thick line shows the error for the poor man's Poisson solver. The comparison was carried out on the grid so as to avoid mixing errors in solving the equation with errors introduced by interpolation etc.

We compared these two Green's functions by solving the Poisson equation for the density contrast

$$= A \frac{r^2}{4} - \frac{3}{2} \exp\left(-\frac{r^2}{2}\right) \quad (28)$$

The solution to the Poisson equation for this source can be obtained analytically and the potential is

$$= \frac{A}{a} \exp\left(-\frac{r^2}{2}\right) + \text{const.} \quad (29)$$

We solved the Poisson equation numerically using the two Green's functions defined above on a  $64^3$  mesh. We computed the *rms* deviation from the true solution in each case for a large range of values for  $\rho$ . The result of this analysis is presented in figure 4 that shows the error as a function of  $\rho$ . This curve clearly shows that the periodic kernel introduces more error than the poor man's Poisson solver.

### 3.3 Computing the Gradient of Gravitational Potential

Numerical differentiation is used to compute the force  $[\mathbf{r}]$  on the mesh. The gravitational potential  $\phi$  is also defined on the mesh. Interpolation is used to compute the force at the particle position.

Here we will discuss three most commonly used methods for computing the gradient of potential in N-Body codes.

The most accurate and fastest method for computing derivatives uses fast Fourier transforms. The Fourier components of force are computed directly from the Fourier components of gravitational potential. Only possible source of errors here is the FFT routine itself. The FFT routine used here gives an error of about  $10^{-4}\%$  for Fourier transforming a sine wave in a  $64^3$  box. [This error was estimated by comparing numerical values of Fourier components with their expected value.]

The expression for Fourier transform of a derivative is

$$f_k^0 = ik \bar{f}_k \quad (30)$$

The simplest method for computing the derivative in real space is the mid point rule.

$$\frac{\partial f}{\partial x} = \frac{f(x+h) - f(x-h)}{2h} + O(h^2) \quad (31)$$

The equivalent expression for computing the derivative on the mesh is

$$\frac{\partial f}{\partial n} = \frac{f(n+1) - f(n-1)}{2} \quad (32)$$

For an individual sine wave, the fractional error varies as  $k^2$  for small  $k$ . Here, as for every operation in cosmological simulations, periodic boundary conditions are used to compute the derivative near the edges.

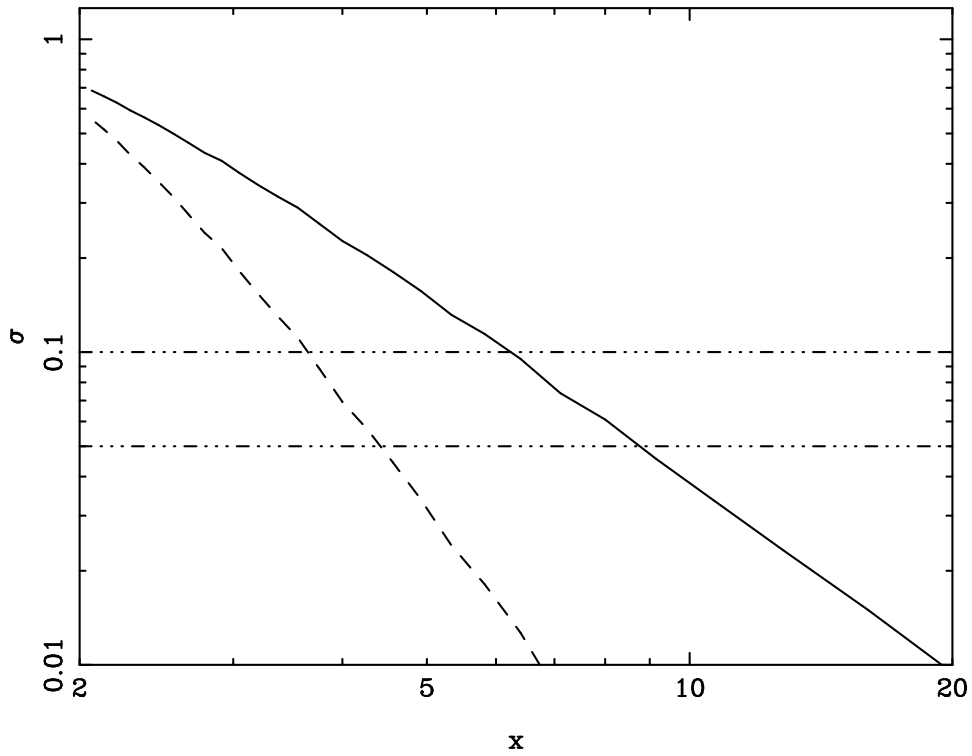


Figure 5: This figure shows *rms* error in numerical differentiation. We differentiated sine waves with frequencies  $k_x$ ,  $k_y$  and  $k_z$  where  $k_i = 2^{-x_i}$ . We then compared the numerical result with its analytical counterpart to obtain an estimate of error. We have plotted the error as a function of  $x = 2^{-x} = (k_x^2 + k_y^2 + k_z^2)^{1/2}$ . Dashed line shows error for the five point formula and the thick line shows error for the mid point rule. Horizontal dot-dashed lines show the 10% and the 5% error level. This error analysis was carried out in a  $64^3$  box.

| Method     | 5% error (k;l) | 10% error (k;l) |
|------------|----------------|-----------------|
| Mid-Point  | 0:7, 9:0       | 1:0, 6:3        |
| Five Point | 1:4, 4:5       | 1:7, 3:7        |

Table 2: This table lists the scale at which error in differentiation crosses the 5% and 10% level for the mid-point and the five point methods. A comparison of these values suggests that the five point method is more robust and less error prone of the two.

It is possible to construct a more accurate formula by using the method of undetermined coefficients [See for example Antia (1991)]. A five point formula for differentiation that gives fractional errors proportional to  $k^4$  for small  $k$  is

$$\frac{\partial f}{\partial x} = \frac{f(x-2h) - f(x+2h) + 8(f(x+h) - f(x-h))}{12h} + O(h^5) \quad (33)$$

This translates into the following expression for a uniformly spaced grid :

$$\frac{\partial f}{\partial n} = \frac{f(n-2) - f(n+2) + 8(f(n+1) - f(n-1))}{12} \quad (34)$$

To compare these methods we studied the variation of relative error for sine waves as a function of frequency. We computed the numerical derivatives of a set of sine waves in a  $64^3$  box and compared these with the analytical results. We have plotted the root mean square error as a function of the inverse of wavenumber  $x = 2\pi/k$  in figure 5. Dashed line shows error for the five point formula and the thick line corresponds to the mid point rule. It is clear from these curves that the five point formula is far more accurate than the mid point rule.

We have listed in table 2 the wavenumber for at which the average error crosses some thresholds for these two formulae.

### 3.4 Tests of Force Calculation

In the preceding subsections we have studied the steps involved in computing the force field for a given distribution of particles. For each step we discussed alternate methods of computing the required quantity and also discussed their relative merits. We shall now discuss the errors in computing the force field for one particle. We will use many combinations of individual components like the interpolating function, Green's function and the differentiator and compare the errors for each combination.

To compute the error we placed a particle at a random position in a given lattice cell and computed force due to this at a fixed distance  $r$  in many directions to obtain the average force. We also computed the rms dispersion about the average. This process was repeated for one hundred positions of the particle in the lattice cell. Errors in this force were computed by comparing with the true  $1/r^2$  force expected in such a situation. The error was split into two parts : transverse and radial. The results of this study may be summarised as follows :

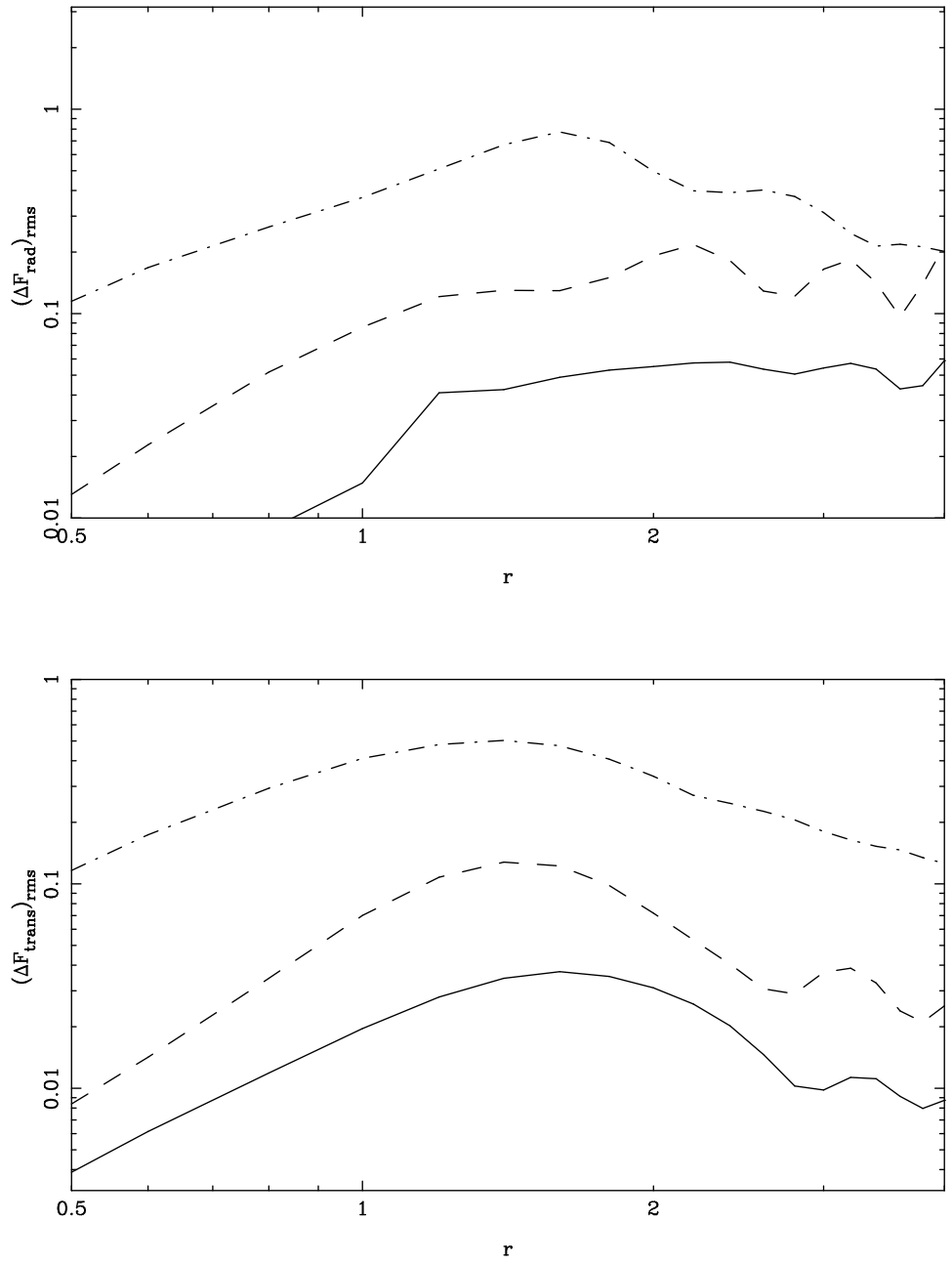


Figure 6: This figure shows the error in force of one particle. The top panel shows the root mean square dispersion in the radial force. The lower panel shows corresponding curves for the transverse component of force. The thick line shows the error for TSC interpolating function, the dashed line for CIC and the dot-dashed line corresponds to NGP. In these panels the potential was computed using the poor man's Poisson solver and the gradient of the potential was computed in the Fourier space.

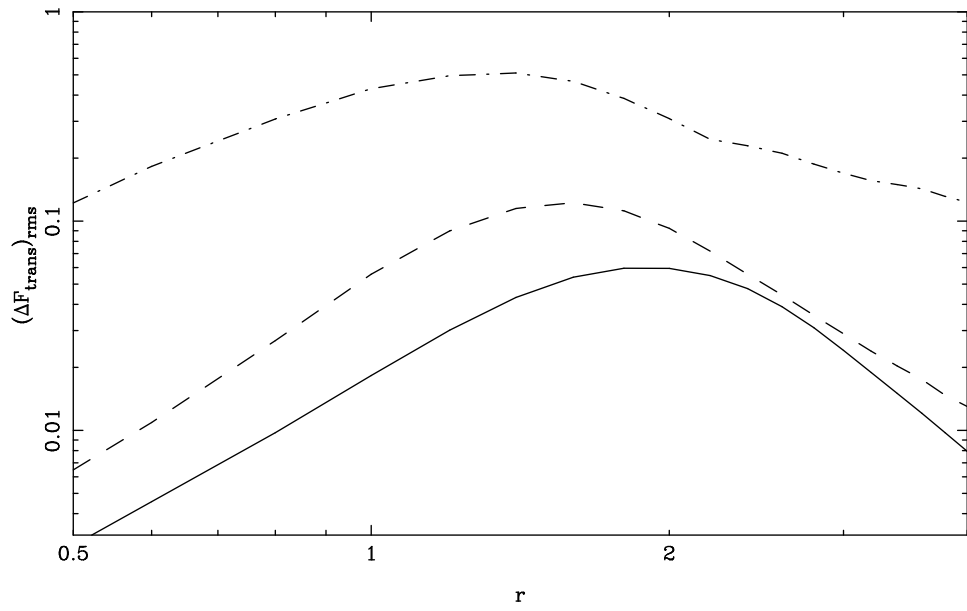
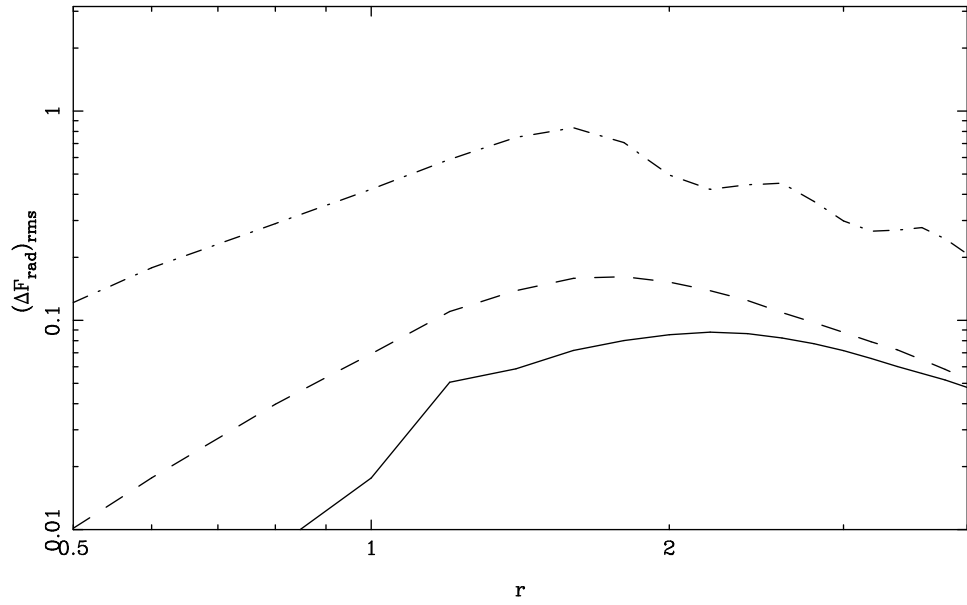


Figure 6: Continued. In these panels the Poisson equation was solved using the periodic Green's function and the mid point formula was used for computing the force. Notice that the CIC and TSC curves converge in this case indicating that the error is dominated by some other component.

The average force deviates very little from the true force for distances larger than one grid length [ $r > L$ ] for almost all combinations of components.

The root mean square dispersion about the average can be large for some combinations of components.

Smallest *rms* dispersion is obtained for the combination of TSC, poor man's Poisson solver and numerical differentiation in Fourier space.

The combination of CIC, periodic kernel and mid point differentiation also gives small errors. Surprisingly the errors in CIC and TSC [other components remaining same] *converge* at scales larger than the grid size. This clearly indicates that the error is dominated by some other component, probably the mid-point differentiation. [Convergence disappears when five point formula or differentiation in Fourier space is used.]

To elucidate some of the points made above we have plotted the radial and transverse error for the two combinations of components mentioned in the last two points. Figure 6 shows that the error is minimum for TSC amongst the three interpolating functions in all the cases. Other points mentioned in the above discussion are also brought out clearly in these panels. We will use the combination of TSC interpolating function and the poor man's Poisson solver. We will compute the gradient of potential in the Fourier space.

## 4 Fast Fourier Transforms

In previous sections we discussed methods used for moving the particles and the steps involved in computing the force in N-Body simulations. We mentioned that fast Fourier transforms are used for computing the Fourier transforms and play a vital role in reducing the time taken in computing the force. In this section we will start with the usual expression for the Fourier transform and reduce it to the form in which it is processed by the FFT. For details of the FFT techniques we refer the reader to any standard book on numerical analysis. (Antia (1991); Press et al. (1986))

For simplicity we will work in one dimension in this section. However we will write the  $d$ -dimensional generalisation of the main result. Consider a function  $f(x)$  that has the Fourier transform  $g(k)$ . Then we may write

$$f(x) = \int_{-\infty}^{\infty} \frac{dk}{2\pi} g(k) e^{ikx} \quad (35)$$

It is not possible to use computers to integrate arbitrary functions over an infinite range in finite time. The integral is thus truncated at some finite  $k_{max}$ . This truncation is possible only for those functions for which the integral over  $|k| > k_{max}$  is sufficiently small. Thus the integral to be evaluated becomes

$$f(x) \approx \int_{-k_{max}}^{k_{max}} \frac{dk}{2\pi} g(k) e^{ikx} \quad (36)$$

This integral is evaluated in form of a summation over the integrand.

$$f(x) = \sum_{k=-k_{max}}^{k_{max}} g(k) e^{ikx} \frac{k}{2} \quad (37)$$

where the function is sampled at intervals of  $k$  in this interval. For a constant  $k$ , this sampling will divide the range  $-k_{max}$  to  $k_{max}$  in  $N$  intervals where  $N = (2k_{max} = k) - 1$ . The fast Fourier transforms require the number of intervals to equal an integer power of 2, which clearly is not possible for the above range if we are to sample the  $k = 0$  mode as well. It is possible to circumvent this problem by making the range of integration asymmetric. We add one extra interval after  $k_{max}$  and thus make the number of intervals equal to an even number. We can further choose  $k_{max}$  and  $k$  to ensure that  $N$  is an integer power of two. Thus the sum may be written as

$$\begin{aligned} f(x) &= \frac{1}{NL} \sum_{k=-k_{max}}^{k_{max} + k} g(k) e^{ikx} \\ &= \frac{1}{NL} \sum_{m=N-2+1}^{N-2} g(k_m) e^{i k_m x} \end{aligned} \quad (38)$$

The boxsize  $NL = 2 = k$  defines the scale over which the function  $f(x)$  is defined apart from its periodic copies. Here  $N = (2k_{max} + k) = k = 2^j$  where  $j$  is a positive integer. The function  $f(x)$  is defined on a regular mesh with  $L$  as the spacing between adjacent mesh points. This allows us to rewrite the previous equation as

$$f(nL) = \frac{1}{NL} \sum_{m=N-2+1}^{N-2} g(k_m) e^{i2 m n/N} \quad (39)$$

To rewrite this in the form used by the FFT algorithm we split this sum into two parts :

$$\begin{aligned} f(nL) &= \frac{1}{NL} \sum_{m=N-2+1}^{N-1} g(k_m) e^{i2 m n/N} \\ &\quad + \frac{1}{NL} \sum_{m=0}^{N-2} g(k_m) e^{i2 m n/N} \end{aligned} \quad (40)$$

Changing the summation index in the first sum by  $N - [m - m + N]$  and dropping a 2 factor in the phase, we obtain

$$\begin{aligned} f(nL) &= \frac{1}{NL} \sum_{m=N-2+1}^{N-1} g(k(m - N)) e^{i2 m n/N} \\ &\quad + \frac{1}{NL} \sum_{m=0}^{N-2} g(k_m) e^{i2 m n/N} \end{aligned} \quad (41)$$

These terms can be put together in the following form

$$f(\mathbf{n}L) = \frac{1}{N^d} \prod_{m=0}^{N-1} G(\mathbf{k}m) e^{i2\pi \mathbf{m} \cdot \mathbf{n}L} \quad (42)$$

where  $G(\mathbf{k}m) = g(\mathbf{k}m)$  for  $m_i \leq N/2$  and  $G(\mathbf{k}m) = g(\mathbf{k}(m - N))$  for  $m_i > N/2$ . From here it is clear that the input array for FFT should have the negative wave numbers *after* the positive wavenumbers. [This can also be interpreted as “periodicity” in  $k$  space.] The generalisation of the above expression to  $d$  dimensions is

$$f(\mathbf{n}L) = \frac{1}{(N^d)} \prod_{m=0}^{N-1} G(\mathbf{k}m) e^{i2\pi \mathbf{m} \cdot \mathbf{n}L} \quad (43)$$

Here  $G(\mathbf{k}m)$  is the Fourier transform of the function  $f(\mathbf{n}L)$  with every component  $m_i > N/2$  replaced by  $m_i - N$ .

If an FFT routine uses a different normalisation then the input array must be rescaled to get the correct amplitude for the function  $f(\mathbf{n}L)$ . If the FFT routine uses

$$f(\mathbf{n}L) = \frac{1}{L^d} \prod_{m=0}^{N-1} G(\mathbf{k}m) e^{i2\pi \mathbf{m} \cdot \mathbf{n}L} \quad (44)$$

then we must scale the input function as  $G^{FFT} = G / (L^d)$ . This scaling is not important if we are computing both the forward and the inverse transform as the overall normalisation must be same for all FFT routines. This scaling becomes relevant only in those cases where we are transforming a given quantity only once, as in the generation of initial potential.

The above equations establish the form in which an array must be passed to the FFT routines in order to compute the Fourier transform.

## 5 Setting up Initial Conditions

### 5.1 The Initial Density and Velocity Field

$N$ -Body simulations are generally started from fairly homogeneous initial conditions, i.e. the density contrast is much smaller than unity at all scales that can be studied using the simulation. In this regime we can use linear theory to compute all quantities of interest.

In linear theory, the evolution of density contrast can be described as a combination of a growing and a decaying mode. We can write the solution for perturbations in an Einstein-deSitter Universe as

$$\delta(\mathbf{a}) = c_1 a + c_2 a^{-3/2} \quad (45)$$

We can evaluate  $c_1$  and  $c_2$  by using the initial conditions. These conditions can be written in terms of the initial velocity field and the initial potential.

$$\frac{\partial \delta_{in}}{\partial a} = -\frac{2}{3} \frac{v_{in}}{a} \quad (46)$$

Using these we can express the linear solution in terms of the initial potential and the initial velocity field as

$$(a) = \frac{3}{5} r_{in}^2 - \frac{2}{5} r_{in} u_{in} a + \frac{2}{5} r_{in}^2 + r_{in} u_{in} a \quad (47)$$

This equation suggests that for a system in growing mode,  $u_{in} = r_{in}$ . This equation gives us the density contrast at each point in terms of the initial gravitational potential. [We will discuss the problem of generating the initial potential in the next subsection.] Given an initial potential the above equation suggests two schemes for generating the initial density field. These are :

The particles are distributed uniformly and their masses are proportional to the local value of density. We can either start with zero velocities, in which case we have to increase the amplitude of  $r_{in}$  by a factor 5/3 to account for the presence of decaying mode. Alternatively we can choose to put the system in the growing mode and assign velocity  $u_{in} = r_{in}$  to each particle. One major drawback of this method is that an extra array containing masses of particles needs to be stored and this can be a problem for large simulations.

Starting with a uniform distribution the particles are displaced by a small amount, say much less than the inter-particle separation, using velocity  $u_{in} = r_{in}$ . The resulting distribution of particles will represent the required density field if the initial distribution did not have any inhomogeneities. We can also retain the initial velocity field.

Thus the main requirement from initial positions of particles before we generate the required perturbation is that the distribution of particles sample the potential “uniformly.” Any inhomogeneities present in the initial distribution will combine with the density perturbations that are generated by displacing particles and will modify the initial power spectrum.

One obvious solution that ensures a uniform distribution is placing particles on the grid. This generates a distribution that is uniform but not random. An additional problem with this distribution is the extreme regularity which leads to shot noise at Nyquist frequency for potentials with large coherence length when the number of particles is smaller than the number of cells in the mesh. [See figure 7]

Another “obvious” solution is to put particles at random inside the simulation box. This distribution is uniform but it has  $\frac{1}{N}$  fluctuations which result in spurious clustering. The fluctuations in number of particles in a cell of size  $R$  decrease as  $1/R^{3/2}$  with scale. [Comparing with power law spectra we note that this is an  $n = 0$  spectrum.]

Apart from these simple minded solutions there exist [at least] two other distributions of particles which may be used for the initial positions.

The *Glass* initial conditions are obtained by running a random distribution of particles through N-Body with a repulsive force. In this case we start with small perturbations and the repulsive force leads to a slow decrease in the amplitude of perturbations. As the perturbations get progressively smaller it worthwhile to estimate the evolution of inhomogeneities using linear theory. The equation for evolution of perturbations in this case is same as the standard equation for linear growth of perturbations (Peebles (1980)) but with a source term that has an opposite sign. This leads to the

following oscillatory solution with a decaying amplitude.

$$\phi(a) = a^{-1/4} \left[ \cos \frac{p\sqrt{23}}{4} \ln a + \sin \frac{p\sqrt{23}}{4} \ln a \right] \quad (48)$$

Where  $\alpha$  and  $\beta$  are constants to be fixed by initial conditions. The process of generating initial conditions can take a long time for a large number of particles. However this has to be done only once and the data can be stored in a file for repeated use.

The other method is a variant of the grid and Poisson initial positions mentioned above. Here particles are placed in lattice cells but at a random point within the cell. This removes the regularity of grid without sacrificing uniformity. The number fluctuation falls faster than  $\frac{1}{\sqrt{N}}$  and have a smaller amplitude even at the smallest scale. The amplitude of fluctuations can be controlled by reducing the amplitude of displacement about the mesh point.

After the initial density field has been generated the initial velocities for N-Body can be set as  $u_{in} = r_{in}$  if we want the system to be in the growing mode. However, generation of density field from the initial potential, as outlined above involves many numerical operations that modify the potential at scales comparable to the mesh size. A better method, for consistency of density, velocity and potential, is to recompute the potential after generating the density field and set the velocities with the recomputed potential (Efstathiou et al. (1985)). This is particularly important in case of models with a lot of small scale power. If we use the initial potential for fixing velocities then velocities have a stronger small scale component than would be expected from the density field that has been generated, leading to inconsistency in the input configuration for N-Body. Therefore we use  $u_{in} = r_{in}$ , where  $r^2 = \phi(a)=a$  is the potential generated from displaced distribution of particles.

## 5.2 Initial Potential

In this section we shall outline the method used to generate the initial potential. The same method can also be used to compute the density field directly if the initial density field is to be generated by placing particles with different masses on the mesh.

In most models of structure formation the initial density field is assumed to be a Gaussian random field. Linear evolution does not modify the statistics of density fields except for evolving the amplitude. As the potential and density contrast are related through a linear equation, it follows that the gravitational potential  $\phi$  is also a Gaussian random field at early epochs.

A Gaussian random field is completely described in terms of its power spectrum. The Fourier components of a Gaussian random field [both the real and the imaginary part] are random numbers with a normal distribution with variance proportional to the power spectrum of the random field. The proportionality constant depends on the Fourier transform convention. To fix this constant we consider the probability functional for a function  $g$ .

$$P[g] = B \exp \left[ -\frac{1}{2} \int \frac{d^3k}{(2\pi)^3} \frac{\tilde{g}(k) \tilde{g}^*(k)}{P_g(k)} \right] \quad (49)$$

Here  $B$  is a normalisation constant. In the Fourier transform convention used in §3 this equation can be written as

$$P[g] = B \exp \left[ -\frac{1}{2} \frac{1}{(NL)^3} \sum_{\text{all } k} \frac{g(k) \bar{g}(k)}{P_g(k)} \right] \quad (50)$$

Thus the variance of the real and imaginary components for each Fourier mode of a Gaussian random field should equal

$$\langle g_{\text{real}}(k) \bar{g}_{\text{real}}(k) \rangle = \langle g_{\text{imag}}(k) \bar{g}_{\text{imag}}(k) \rangle = \frac{P_g(k) N^3 L^3}{2} \quad (51)$$

The factor of 2 takes into account the fact that both the real and the imaginary components share the variance. Thus the function  $g$  may be written as

$$g(k) = (a_k + ib_k) \frac{P_g(k) N^3 L^3}{2} \quad (52)$$

where  $a_k$  and  $b_k$  are Gaussian random numbers with zero mean and unit variance.

To generate the gravitational potential we substitute the gravitational potential  $\phi_k$  in place of  $g(k)$  and the power spectrum with the power spectrum for the gravitational potential. The power spectrum for the gravitational potential is  $P(\phi; a) = P(\phi; a) = (a^2 k^4) = P^{\text{lin}}(a=1; k) = k^4$ . Here  $P^{\text{lin}}(a=1; k)$  is the linearly extrapolated power spectrum of density fluctuations. With this, we can write

$$\phi_k = (a_k + ib_k) \frac{P^{\text{lin}}(a=1; k) N^3 L^3}{2k^4} \quad (53)$$

Here we have taken  $a(t_0) = 1$ . To specialise to the Fourier transform convention used in the FFT routine we use, we use  $l = N^{1/2}$ . [eqn.(44)] This implies

$$\phi_k^{\text{FFT}} = \frac{k}{N^{3/2} L^3} = (a_k + ib_k) \frac{P(\phi; k)^{1/2}}{2L^3 k^4} \quad (54)$$

Here  $k = 2\pi m / (NL)$ . If  $P(\phi; k)$  is of the form  $A k^n f(k)$  where  $f$  is a dimensionless function [It may be the transfer function or a cutoff imposed by hand.] and  $A$  is the amplitude. In the units we are using here  $L = 1$ , therefore

$$\phi_m^{\text{FFT}} = (a_m + ib_m) \frac{A}{2} \frac{2\pi m}{N} \frac{N^{-4}}{f} \frac{2\pi m}{N} \quad (55)$$

where all lengths are written in units of  $L$ .

### 5.3 Testing Initial Conditions

In this section we shall test the initial conditions generated by the method outlined above. We will compare the power spectrum of density perturbations generated by this method with the theoretical

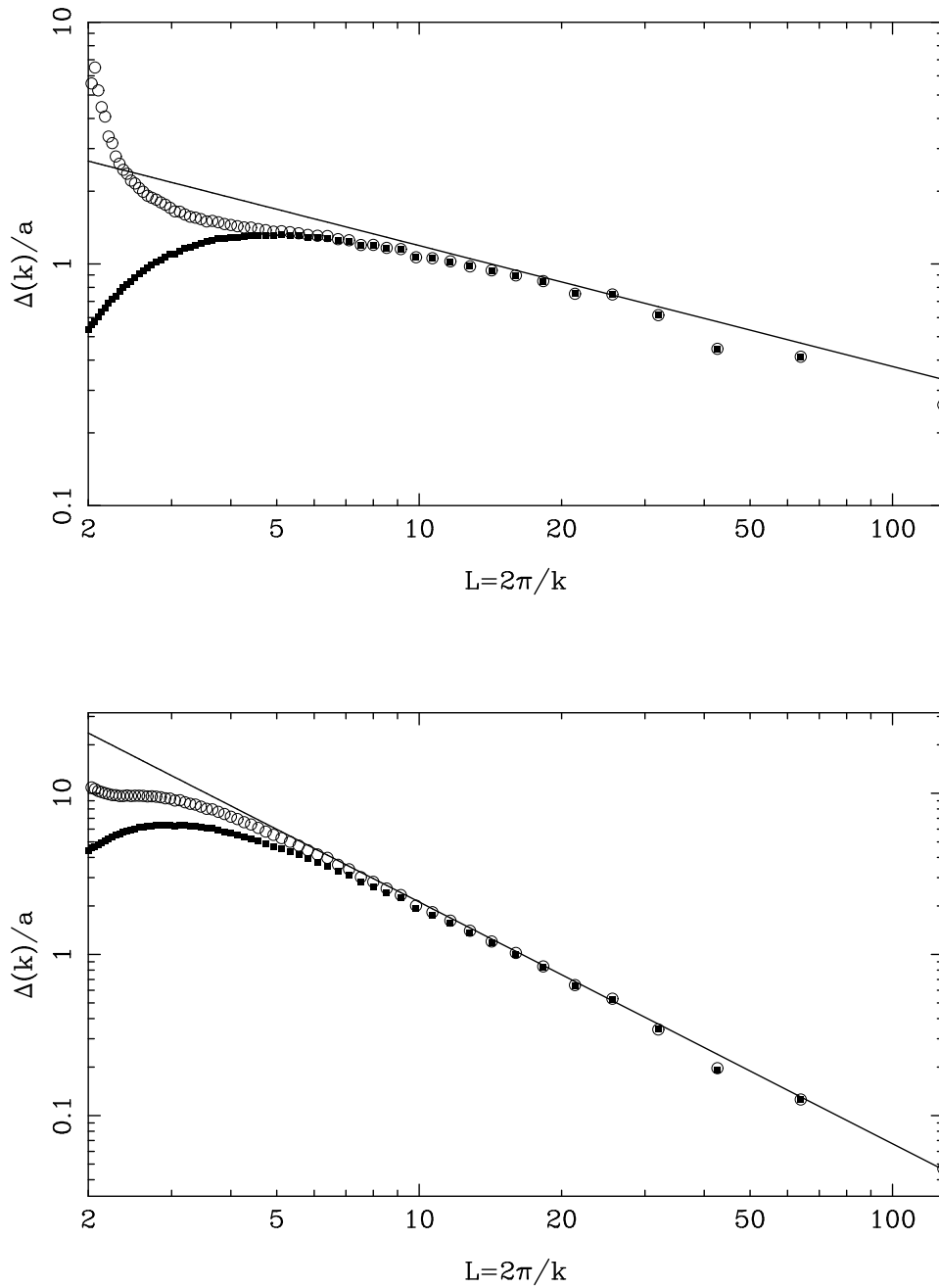


Figure 7: This figure shows the theoretical power spectrum and the induced power spectra, linearly extrapolated to  $a = 1$ . The theoretical power spectrum is shown as a thick line and the power spectrum generated by displacing the particles is shown as filled squares [for simulations with  $128^3$  particles] and as empty circles [for simulations with  $64^3$  particles]. The upper panel here corresponds to the power law model with  $n = 2$  and lower panel to the model with  $n = 0$ .

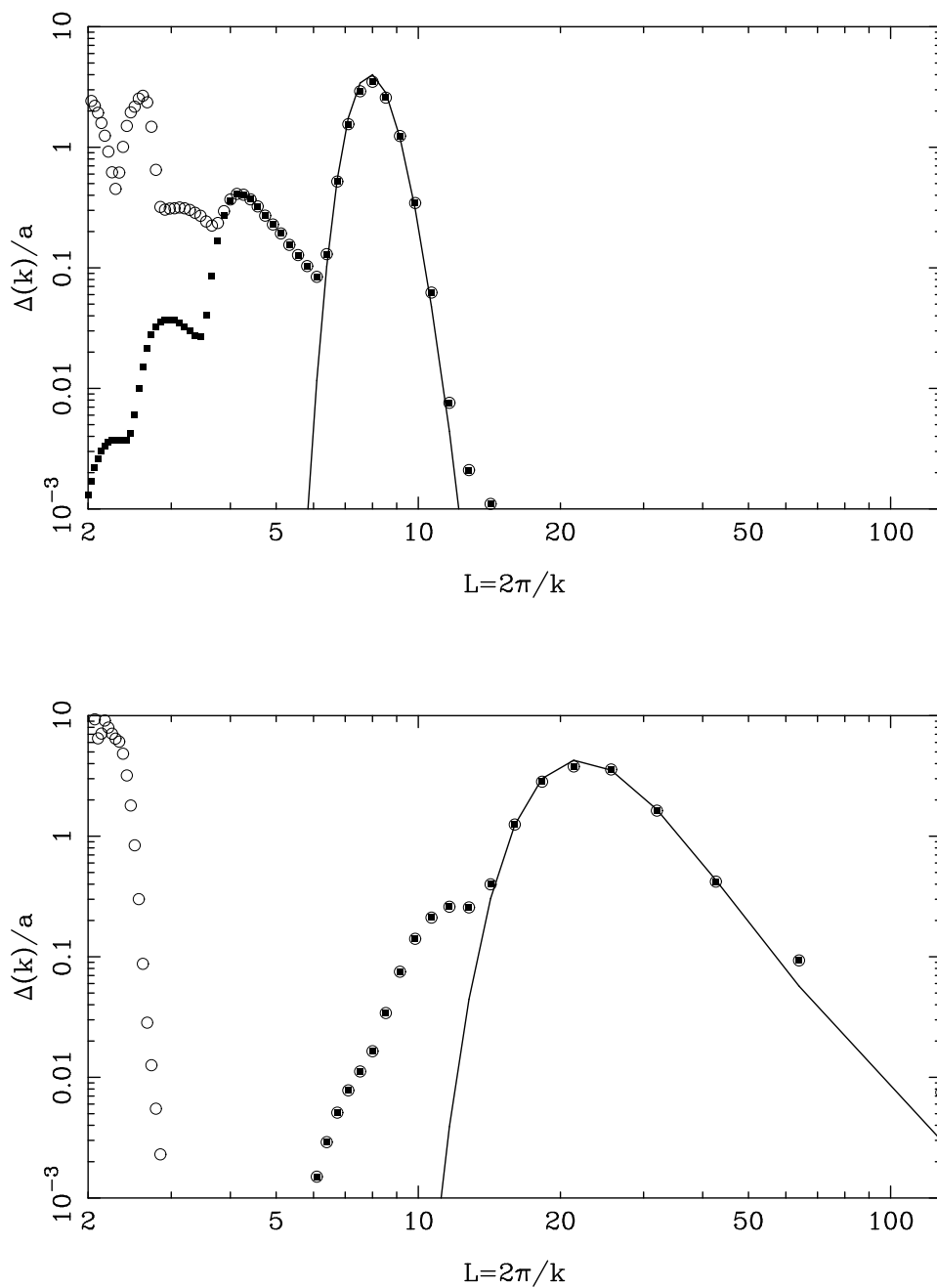


Figure 7: Continued. These panels show the initial power spectra for models with Gaussian power spectrum. The upper panel corresponds to a Gaussian power spectrum with peak at  $L_0 = 8L$  and the lower panel corresponds to a spectrum with  $L_0 = 24L$ . The secondary peaks at small scales occur at the harmonics of the wavenumber corresponding to the peak of the initial Gaussian.

power spectrum for a wide range of models. This comparison was carried out using simulations done with  $128^3$  particles in a  $128^3$  box. To study the effect of a smaller number of particles we also studied the power spectrum for a simulation with  $64^3$  particles in a  $128^3$  box. We use the following models for this purpose :

Power law models with  $n = 2$  and  $n = 0$ .

A Gaussian power spectrum with spread  $k = 2 \Rightarrow N L$  peaked at  $k_0 = 2 \Rightarrow L_0$ .  $[P(k) / \exp f (k - k_0)^2 = 2 \frac{2}{k} g]$  This model was studied for  $L_0 = 8$  and  $24$ .

Models outlined in the first item have power at all scales whereas for the Gaussian power spectrum the power is concentrated in a narrow range of scales. This tests the accuracy of initial condition generation for the two extreme classes of models.

We have plotted the theoretical power spectrum and the induced power spectra, linearly extrapolated to  $a = 1$ , in figure 7 for the models listed above. The theoretical power spectrum is shown as a thick line and the power spectrum generated by displacing the particles is shown as filled squares for simulations with  $128^3$  particles and as empty circles for simulations with  $64^3$  particles.

The simulated power spectrum agrees with the theoretical power spectrum for scales larger than about  $5L$  for power law models. In this range the power spectrum in simulations with different number of particles also agrees quite well.

In case of Gaussian power spectrum the simulated power spectra also contain some power at harmonics of the main peak, i.e., at scales  $L_0=2, L_0=3$ , etc. The Gaussian at scale  $L_0$  is reproduced quite well. Simulations with  $64^3$  particles contain spurious noise around the Nyquist scales. Apart from this difference power spectra in two cases agree quite well.

Simulations with  $64^3$  particles generally have more noise at smaller scales. For hierarchical models this is essentially shot noise. However for models with large scale coherence [as in case of Gaussian power spectrum with  $L_0 = 24L$  or  $n = 2$  power law model] this can lead to large spurious noise at the Nyquist scale. This can be understood in terms of the large coherence length in the displacement field for such models, which leads to a sequence of alternately filled and empty cells. This contributes to the excess noise at the Nyquist scale.

The theoretical power spectrum is reproduced correctly in a large range of scales for a wide variety of models. Power spectrum at scales smaller than about  $5L$  does not match with the theoretical power spectrum and hence results in this regime should not be used at early times. This constraint applies to all types of N-Body codes as the same method is used to generate the initial conditions for all types of N-Body codes. This constraint does not apply at late times as the power at small scales at late times is dictated by initial power at larger scales. (Bagla and Padmanabhan (1997))

## 6 Tests of N-Body Code

In this section we will test performance of the N-Body code as a whole. We will compare the evolution of gravitational clustering in N-Body simulations with analytical results. The number of analytical results available in the non-linear regime is very limited, and hence the number of tests is also very small.

| $k=k_f$ | x     | v     |
|---------|-------|-------|
| 1       | 0.021 | 0.034 |
| 2       | 0.048 | 0.073 |
| 4       | 0.104 | 0.138 |

Table 3: This table lists the errors in positions and velocities for one dimensional collapse. The errors are computed by comparing with Zel'dovich approximation. The errors have been listed for three different initial perturbations, the first column contains the wavenumber[in units of the fundamental wavenumber  $k_f = 2 \pi N$ ] of the sine wave perturbation. The errors were computed at the time of first shell crossing in the system. The N-Body simulation used for this was carried out using  $64^3$  particles.

As a test of evolution of positions and velocities we can compare the motion for a one dimensional collapse before shell crossing with Zel'dovich approximation (Zel'dovich (1970)). This test was suggested by Efstathiou et al.(1985) and they compared the positions and velocities for such a collapse with the corresponding quantities in Zel'dovich approximation. They chose a sine wave along one of the coordinate axes as the initial perturbation in potential. Recently (Melott et al. (1997)) this test has been generalised so that the plane wave is not along any coordinate axis. In such a case the particles can approach each other with a small nonzero impact parameter. Monitoring velocities along directions perpendicular to the perturbation provides a good test of collisionless evolution. Collisionless evolution of a one dimensional perturbation can not induce velocities along directions orthogonal to the perturbation. The authors find that Particle mesh codes are the only ones that pass this test.  $P^3M$  and tree codes can also provide collisionless evolution if the softening length is of the same order as the inter particle separation.

We carried out this test with one dimensional perturbation along the x axis. The results are listed in table 3. Here we have tabulated the root mean square error in displacement and velocity. These are defined here as

$$\begin{aligned}
 x &= \sqrt{\frac{1}{N} \sum_i (x_i - x_i^Z)^2} \\
 v &= \sqrt{\frac{1}{N} \sum_i (v_i - v_i^Z)^2}
 \end{aligned} \tag{56}$$

The table lists errors for three wavenumbers. In each case we have given the error at the epoch of first shell crossing in the system. The error increases with the wavenumber of the sine wave used for initial potential as we sample a given wave with a smaller number of particles and the discretisation effects become more important.

The above test checks the working of an N-Body code for a very special case. In a more general situation it is difficult to compare the output of numerical simulation at the level of positions of

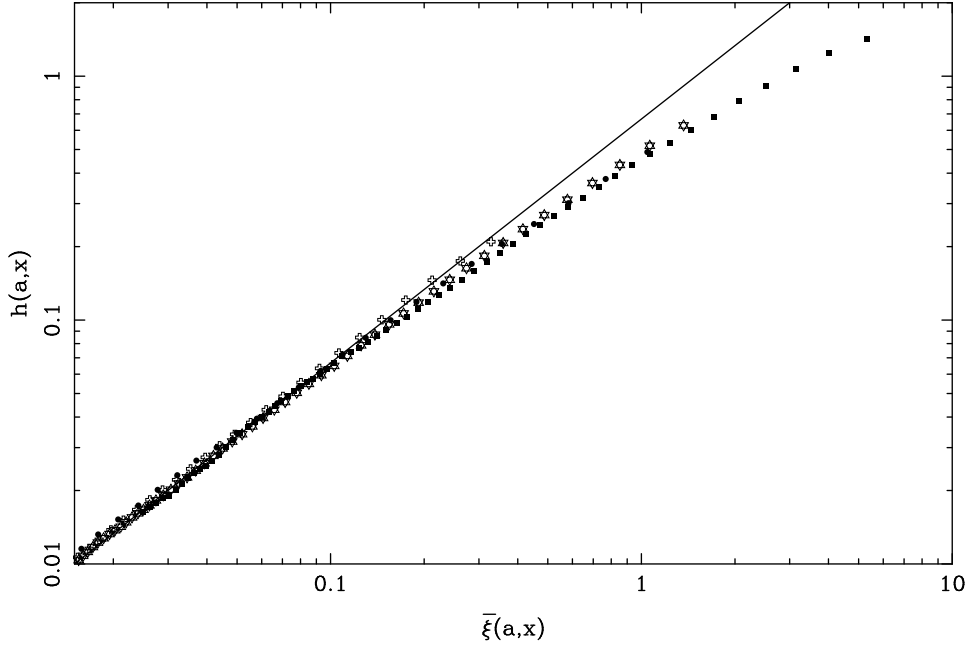


Figure 8: This figure shows  $h(a; x)$  as a function of  $\xi(a; x)$  for two power law models [ $n = 0$  and  $-1$ ] and the CDM model. The thick line depicts the relation between these quantities in linear theory and the results from simulations are shown as points. All the points in the range  $\xi(a; x) \leq 1$  lie along the line with little dispersion.

particles and only a statistical comparison is possible. We will use the averaged correlation function  $\xi(x; a)$  and the scaled pair velocity  $h$  (Peebles (1980)) for testing the accuracy of the N-Body code.

In linear regime the averaged correlation function evolves as  $a^2$ , i.e.,  $\xi(x; a) = (a^2/a_1^2) \xi(x; a_1)$ . In addition we know that  $\xi(x; a) \ll 1$  in this regime. These can be used, along with the pair conservation equation Peebles (1980) to show that  $h = 2/3$  for  $\xi \ll 1$ . This equation is valid for all models in linear theory. We have plotted  $h(a; x)$  as a function of  $\xi(a; x)$  in figure 8. We have plotted the line corresponding to the linear theory result and have shown results from N-Body simulations as points. We used simulations of power law models [ $n = 0$  and  $-1$ ] and the standard CDM model for this plot. Points corresponding to different simulations have been shown with different symbols. All the points crowd around the line  $h = 2/3$  in the linear regime with little dispersion. The points deviate from this line for large  $\xi$  but the dispersion between different models remains small. This corresponds to an approximate “universality” in the relation between  $h$  and  $\xi$ . [Hamilton et al. (1991); Nityananda and Padmanabhan (1994)]

Self similar evolution of  $\xi$  for power law models (Peebles (1980)) can be used to test correctness of the non-linear evolution of gravitational clustering. In figure 9 we have plotted  $\xi(a; x)$  as a function of  $x=x_{n1}$  for the  $n = 0$  power law model. Here  $x_{n1}$  is the scale where the linearly extrapolated  $\xi$  is unity. This scale is proportional to  $a^{2/3}$  for the  $n = 0$  power law model. If the evolution is

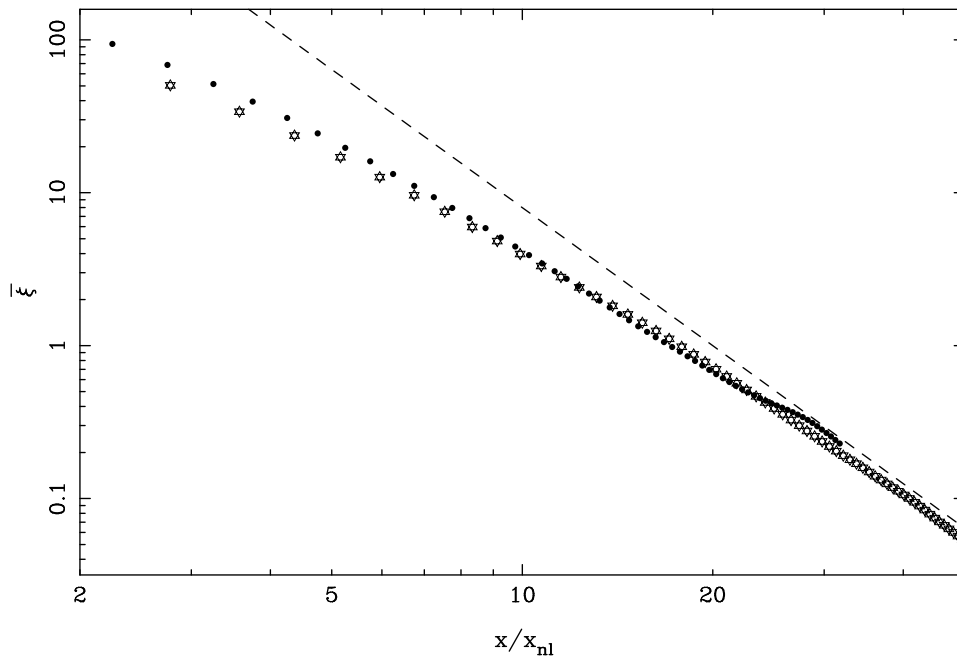


Figure 9: This figure shows  $\xi(x)$  as a function of  $x/x_{nl}$  for the  $n = 0$  power spectrum. The points have been plotted for two epochs. The overlap between points clearly shows that the system is evolving in a self similar manner. The dashed line shows the linear slope of the averaged correlation function.

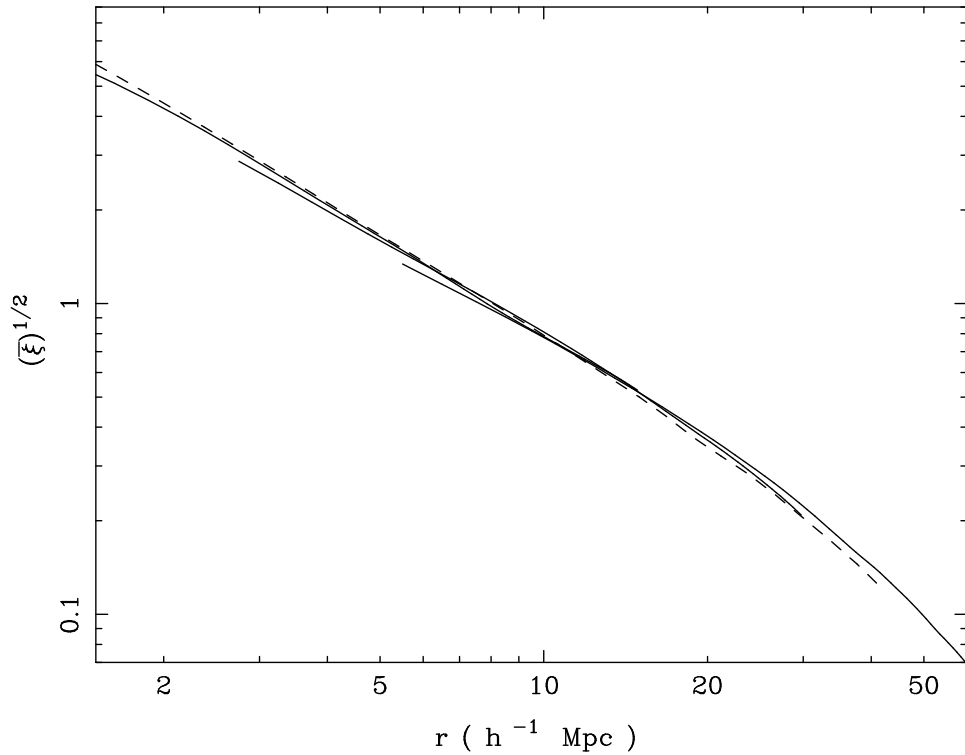


Figure 10: Comparison of simulations at different scales. This figure shows  $\xi^{1/2}$  for three CDM simulations done with boxsize of 64, 128 and  $256h^{-1}\text{Mpc}$ . Matching of curves in the overlapping region shows that the numerical simulation is not introducing any artifacts. The dashed line shows the same function from a  $P^3M$  simulation by Brieur et al.(1995). This simulation was done with the same initial power spectrum but a different realisation of the Gaussian random field was used. The similarity between  $\xi^{1/2}$  in the three PM simulations and the  $P^3M$  simulation shows that the non-linear evolution is being followed in the same manner in both the simulations.

self-similar then the points from different epochs must lie along a single curve. Figure 9 clearly shows that the evolution of averaged correlation function follows a self similar pattern over a large range of scales.

The last test we consider here compares the averaged correlation function for simulations of the standard CDM model. We compare  $\xi^{1/2}$  for three simulations carried out with boxsize 64, 128 and  $256h^{-1}\text{Mpc}$ . Figure 10 shows that the curves match in the overlapping region, implying that the numerical simulation is not introducing any scale in the non-linear evolution of density perturbations. We also compare these curves with  $\xi^{1/2}$  obtained from a different simulation. This reference simulation was done by Brieur, Summers and Ostriker (1995) using a  $P^3M$  code implemented on a GRAPE machine. This simulation was done with the same theoretical power spectrum but using a different realisation of the initial density field. The two types of simulations being compared have

virtually nothing in common as far as the implementation of the mathematical model is concerned. The similarity in these curves implies that both the codes are evolving density perturbations in the same manner.

## 7 Analysis of N-Body Data

In this section we will outline the method used for computing the correlation function and the scaled pair velocity (Peebles (1980)) from simulation data.

The averaged pair velocity  $h$  is defined as

$$\begin{aligned}
 h(a; x) &= \frac{\sum_{i \neq j} a \frac{dx_i}{da} \frac{dx_j}{da} : (x_i - x_j)^2}{\sum_{i \neq j} (x_i - x_j)^2} \\
 &= \frac{\sum_{i \neq j} a \frac{dx_i}{da} \frac{dx_j}{da} : (x_i - x_j)}{\sum_{i \neq j} 1}
 \end{aligned} \tag{57}$$

In this equation subscripts label particles and the averaging is over all pairs with separation equal to  $x$ , i.e.,  $x^2 = (x_i - x_j)^2$ . This quantity is computed from simulation data by binning the pairs by pair separation  $x$ . The number of pairs in a given bin as well as the quantity to be averaged is summed for each pair in each bin. The ratio of these quantities for each bin gives the value of  $h(a; x)$ .

The correlation function was defined in §1.4 as the Fourier transform of the power spectrum. This is equivalent to the following definition

$$\langle a; x \rangle = \frac{1}{N} \sum_{i \neq j} \langle a; y \rangle \langle a; z \rangle \tag{58}$$

where the average is over all pairs of points with separation  $x$  and over all  $x$  with the same magnitude. This can be rewritten as

$$\begin{aligned}
 \langle a; x \rangle &= \frac{\langle a; y \rangle}{\langle a \rangle} \frac{\langle a; z \rangle}{\langle a \rangle} \\
 &= \frac{\langle a; y \rangle \langle a; z \rangle}{\langle a \rangle^2}
 \end{aligned} \tag{59}$$

Here we have used the fact that density contrast is a random field with zero mean. We can replace the densities by number densities and the product of number densities at points separated by a given distance by the number of pairs with that separation. With this the above equation reduces to

$$\langle a; x \rangle = \frac{n(a; x)}{n(a)} \tag{60}$$

where  $n(a; x)$  is the number of pairs with separation  $x$  and  $n$  is the number of pairs in a uniform distribution. Therefore the problem is again reduced to computing the number of pairs separated by

a given distance. This is done by dividing the range of  $x$  into small intervals and binning the pairs into these intervals. Similar operation is required for computing the scaled pair velocity, therefore the binning operation for computing these quantities can be combined conveniently.

We can obtain an expression for the averaged correlation by averaging

$$\begin{aligned}
 \langle a; x \rangle &= \frac{3}{x^3} \int_0^x dy y^2 \quad \langle a; y \rangle = \frac{\int_0^x dy y^2 \langle a; y \rangle}{\int_0^x dy y^2} \\
 &= \frac{\int_0^x dy n(y)}{\int_0^x dy n(y)} = 1
 \end{aligned} \tag{61}$$

where we have used the fact that the average number of pairs with a given separation is proportional to the square of the separation for a uniform distribution of particles. In the discrete realisation of this expression the integrals over number of pairs are replaced by summation over bins. Computationally this quantity is less error prone than the correlation function as for large separations the number of pairs in a given bin in the simulation output approaches the number of pairs for a uniform distribution. Subtracting two nearly equal numbers can give large error. However, in case of the averaged correlation function the excess number of pairs at small scales is carried over to large scales through summation over all smaller scales. And in general the ratio  $\langle n \rangle_P = \langle n \rangle$  is larger at all scales in comparison with  $n = n$ .

## 8 Discussion

In the preceding sections we have described the basic mathematical model that is implemented in particle mesh cosmological N-Body codes. We have not discussed the P<sup>3</sup>M codes, tree codes, etc. in this review as only PM codes are known to ensure collisionless evolution (Melott et al. (1997)) though they suffer from a very limited resolution. Other methods improve spatial resolution but do not ensure collisionless evolution. However, most of the the machinery is common to these codes and many of the results can be carried over to these codes.

## ACKNOWLEDGEMENTS

Authors thank S.F.Shandarin and F.R.Bouchet for useful discussions on many aspects of N-Body codes. JSB thanks CSIR India for the Senior Research Fellowship.

## References

- Bagla J.S. and Padmanabhan T. 1997, MNRAS 286, 1023, (astro-ph/9605202)
- Antia H.M. 1991, *Numerical Methods for Scientists and Engineers*, Tata McGraw Hill
- Barnes J. and Hut P. 1986, Nature 324, 446

Bertschinger E., Gelb J.M. 1991, *Computers in Physics* 5, 164

Bouchet F.R., Adams J.C. and Pellat R. 1984, *A&A* 144, 413

Bouchet F.R. and Kandrup H. 1985, *ApJ* 299, 1

Bouchet F.R. and Hernquist L. 1988, *ApJS* 68, 521

Briau P.P., Summers F.J. and Ostriker J.P. 1995, *ApJ* 453, 566

Dmitriev N.A. and Zel'dovich Ya.B. 1964, *Soviet Phys JETP*, 18, 793

Efstathiou G., Davis M., Frenk C.S. and White S.D.M. 1985, *ApJS* 57, 241

Hamilton A.J.S., Kumar P., Edward Lu and Matthews A. 1991, *ApJ* 374, L1

Hernquist L., Bouchet F.R. and Suto Y. 1991, *ApJS* 75, 231

Hockney R.W. and Eastwood J.W. 1988, *Computer Simulations using Particles*, IOP publ.

Irvine W.M. 1961, Doctoral dissertation, Harvard University

Klypin A.A. and Shandarin S.F. 1983, *MNRAS* 204, 891

Layzer D. 1963, *ApJ*, 138, 174

Melott A.L., Shandarin S.F., Splinter R.J. and Suto Y. 1997, *ApJL* 479, 79

Nityananda R. and Padmanabhan T. 1994, *MNRAS* 271, 976

Peebles P.J.E. 1980, *Large Scale Structure of the Universe*, Princeton University Press

Press W.H., Flannery B.P., Teukolsky S.A. and Vetterling W.T. 1986, *Numerical Recipes*, Cambridge University Press

Suisalu I. and Saar E. 1996, Submitted to *MNRAS*

Wright E.L., Bennet C.L., Gorski K., Hinshaw G. and Smoot G.F. 1996, *ApJ* 464, L21

Zel'dovich Ya.B. 1970, *A&A* 5, 84

